JOURNAL OF PROPULSION AND POWER
Vol. 29, No. 3, May–June 2013

# Mechanical Erosion of Graphite Nozzle in Solid-Propellant Rocket Motor

Piyush Thakre,* Rajesh Rawat,† and Richard Clayton‡
*CD-adapco, Ltd., Melville, New York 11747*
and
Vigor Yang§
*Georgia Institute of Technology, Atlanta, Georgia 30332-0150*

DOI: 10.2514/1.B34630

**A detailed theoretical/numerical framework is established to study the mechanical erosion of graphite-nozzle materials in solid rocket motors with aluminized ammonium perchlorate/hydroxyl-terminated polybutadiene composite propellants. The analysis is based on a combined Eulerian–Lagrangian approach for treating multiphase motor flowfields. The multicomponent reacting gas-phase dynamics is formulated using the conservation equations of mass, momentum, and energy in the Eulerian framework. Turbulence closure is achieved using the standard $k$-$\varepsilon$ two-equation model. The dispersed phase, consisting of aluminum and alumina droplets, is treated in the Lagrangian framework. Combustion of aluminum droplets to aluminum-oxide smoke is considered. Two empirical correlations are first calibrated and then employed to predict the mechanical-erosion rate of the nozzle surface. The estimated erosion rates fall within the range of the available experimental data. Mechanical erosion is prevalent in the convergent section of the rocket nozzle due to the particle impingement on the nozzle surface. No such erosion, however, is observed at the nozzle throat or downstream because the droplet trajectories move away from the nozzle surface in those regions.**

## Nomenclature

$c_p$ = specific heat
$D$ = droplet diameter
$E$ = specific total energy
$E_f$ = mechanical-erosion rate, $\mathrm{kg/m^2/s}$
$e_r$ = erosion ratio
$h$ = enthalpy
$p$ = pressure
$p_o$ = chamber pressure
$T$ = temperature
$T_o$ = chamber temperature
$U$ = velocity
$V$ = volume
$\mathbf{v}$ = velocity vector
$X_i$ = mole fraction of species $i$
$\alpha$ = particle incidence angle
$\rho$ = density

*Subscript*

$p$ = particle phase

## I. Introduction

GRAPHITE and carbon–carbon composites, which are widely used as rocket-nozzle materials, undergo significant erosion at high chamber pressures and temperatures [1,2]. The increase in the nozzle area from such erosion can reduce the motor performance significantly. The nozzle-surface recession rate should thus be taken into account to accurately predict the performance of a motor. It is important to characterize and minimize nozzle erosion to withstand severe operating conditions. In the case of nonmetalized solid propellants [e.g., ammonium perchlorate (AP)/hydroxyl-terminated polybutadiene (HTPB)], the surface recession is attributed to the chemical erosion caused by heterogeneous reactions between the nozzle material and oxygen-containing combustion products [e.g., water ($H_2O$), hydroxyl group, and carbon dioxide ($CO_2$)]. In the case of metalized solid propellants [e.g., AP/aluminum (Al)/HTPB], however, there could be mechanical erosion at certain nozzle sections in addition to chemical erosion.

The mechanical erosion of a solid rocket-motor nozzle results from the impingement of condensed-phase aluminum-oxide ($Al_2O_3$) (alumina) particles on the nozzle surface. Such erosion has been found to be prevalent in the convergent section of the nozzle, especially for submerged nozzles [3,4]. Comprehensive theoretical/numerical models have been developed previously by the authors to predict [5–7] and mitigate [8] the chemical erosion of a nozzle surface. Several numerical studies [9–12] were carried out using an Eulerian–Lagrangian approach to account for the effect of alumina particles on the motor flow dynamics. There was, however, either no treatment [9,10] or limited qualitative treatment [11,12] of the mechanical erosion of a rocket nozzle. A detailed analysis is yet to be developed to quantify such a phenomenon. A step in this direction will be extremely valuable in achieving an improved understanding of the behavior of nozzle erosion in its entirety.

During the combustion of aluminized composite propellants such as AP/Al/HTPB, a significant fraction of the Al may remain unreacted at the propellant surface. Those unreacted Al particulates, in their liquid form, coalesce to form agglomerates in the order of 100 $\mu$m. Owing to the low volatility, they do not burn instantaneously at the surface, but continue to vaporize and burn slowly when traversing the motor [9]. The vaporized Al reacts with the oxidizing species in the gas phase, forming $Al_2O_3$ smoke. While some part of the $Al_2O_3$ smoke diffuses away from the burning surface, some of it condenses onto the Al droplets to form an oxide-shell cap. Consequently, there exist typically two different types of droplets in the motor: single-component Al and multicomponent $Al/Al_2O_3$

---

Presented as Paper 2010-615 at the 48th AIAA Aerospace Sciences Meeting Including the New Horizons Forum and Aerospace Exposition, Orlando, Florida, 4–7 January 2010; received 30 March 2012; revision received 31 August 2012; accepted for publication 7 September 2012; published online 22 March 2013.

*Ph.D., Senior Development Engineer; piyush.thakre@cd-adapco.com (Corresponding Author).

†Ph.D., Director of Combustion and Reacting Flows.

‡Director of CFD Technology.

§William R. T. Oakes Professor and Chair, School of Aerospace Engineering; vigor@gatech.edu. Fellow AIAA.

droplets. The presence of the $Al_2O_3$ oxide-shell cap slows and prevents the further oxidation of the Al. In comparison, the reaction rate of pure Al droplets is much more rapid and is considered to be diffusion controlled. The combustion of Al droplets thus results in a bimodal size distribution of $Al_2O_3$ particles in the chamber. The droplets consist mainly of submicron $Al_2O_3$ mist (80–90% of mass) that can be modeled as part of the continuous phase. The remaining $Al_2O_3$ droplets range from 20 to 200 $\mu$m, depending on the original Al particle size and the degree of agglomeration [9,10]. The presence of $Al/Al_2O_3$ droplets may lead to a loss of motor performance by causing the mechanical erosion of the nozzle or by increasing the two-phase flow loss in the motor. Their presence, on the other hand, may reduce combustion instability in the motor by offsetting the driving mechanisms that lead to flow oscillations [13,14]. The effects of the dispersed phase on motor performance with respect to combustion instabilities and slag accumulation are addressed in [15].

On the course of their trajectories, the $Al/Al_2O_3$ particles impact the nozzle surface and gradually remove some nozzle materials through repeated deformations and cutting actions. Mechanical erosion due to particle impact is often encountered in a number of mechanical devices. A common example is the erosive wear associated with the movement of slurries through piping and pumping equipment. Mechanical erosion is also observed in gas-turbine blades. The rate of erosive wear is dependent upon several factors. In addition to the properties of the surface being eroded, the material characteristics of particles, such as their shape and hardness, along with the impact velocity and impingement angle, play dominant roles. The impingement angle is widely recognized as one of the most important factors. For ductile materials, the maximum wear rate occurs when the impingement angle is approximately 30 deg. For nonductile materials, however, the wear becomes most severe when the impingement angle is normal to the surface.

The purpose of the current work was to conduct a comprehensive numerical study of mechanical erosion of graphite-nozzle materials. First, a thorough analysis is carried out to obtain the distributions of multiphase flow properties in a practical solid rocket motor. Detailed information is obtained about the near-surface thermo-fluid dynamics and particle trajectories to allow for a high-fidelity investigation into the nozzle-material erosion. The second step involves the modeling of the mechanical erosion due to the impingement of $Al/Al_2O_3$ droplets. The mechanical erosion of the nozzle is then characterized and quantified by using calibrated correlations available in the literature.

## II. Theoretical Formulation

For the aluminized AP/HTPB propellant, the multicomponent gas flow inside the motor is composed mainly of $H_2O$, $Al_2O_3$, Al, $CO_2$, hydrogen chloride (HCl), carbon monoxide (CO), nitrogen ($N_2$), and hydrogen ($H_2$) [16,17]. Condensed-phase particles [$Al/Al_2O_{3(l)}$ and $Al_{(l)}$] are also present. A multiphase treatment of the motor internal flow is thus necessary. For systems that consist mainly of a single continuous phase carrying a relatively small volume of discrete particles, the Eulerian–Lagrangian multiphase model can be used to calculate the trajectories of representative parcels of the discrete phase [9–12,14]. Such an analysis treats the particle size and composition as some of the attributes assigned to the computational particles. It is easier and more economical than with an Eulerian–Eulerian analysis to account for changes in the particle size and composition due to particle combustion. The Eulerian–Lagrangian approach is particularly suited where the interaction of the discrete phase with physical boundaries is important, such as in the current case.

In the Lagrangian/Eulerian framework for multiphase simulations, governing equations for the continuous phase are expressed in the Eulerian form. The model incorporates an arbitrary number of dispersed phases, each modeled in a Lagrangian framework. The state of each particle is updated according to the imposed physical conditions. The Lagrangian phase is influenced by that of the continuous phase and vice versa, through interphase mass, momentum, and energy-transfer effects. The theoretical formulation involves the general conservation laws for both the continuous (gas) and discrete (particle) phases.

### A. Continuous Phase

The gas-phase dynamics is modeled using the conservation equations of mass, momentum, energy, and species concentration. The coupled flow model available in the commercially available computational fluid dynamics (CFD) code STAR-CCM+ [18] is used. The model treats the conservation equations for a multicomponent fluid mixture simultaneously using a time-marching approach. Inter-equation coupling is fully maintained between all equations in the system, including species transport with respect to the momentum and energy conservation, and vice versa. The governing equations in the Cartesian integral form, for an arbitrary control volume $V$ with a differential surface area $da$, are given by

$$\frac{\mathrm{d}}{\mathrm{d}t}\int_V W\,\mathrm{d}V + \oint[\mathrm{F}-\mathrm{G}]\cdot \mathrm{d}a = \int_V H\,\mathrm{d}V \tag{1}$$

in which

$$\mathbf{W} = \begin{bmatrix} \rho \\ \rho\mathbf{v} \\ \rho E \end{bmatrix} \qquad \mathbf{F} = \begin{bmatrix} \rho\mathbf{v} \\ \rho\mathbf{v}\otimes\mathbf{v} + p\mathbf{I} \\ \rho\mathbf{v}\mathbf{H} \end{bmatrix}$$
$$\mathbf{G} = \begin{bmatrix} 0 \\ \mathbf{T} \\ \mathbf{T}\cdot\mathbf{v} + \dot{\mathbf{q}}'' \end{bmatrix} \qquad \mathbf{H} = \begin{bmatrix} 0 \\ \mathbf{f} \\ 0 \end{bmatrix} \tag{2}$$

and $\rho$, $\mathbf{v}$, and $p$ are the density, velocity, specific total energy, and pressure of the fluid, respectively. $\mathbf{T}$ is the viscous stress tensor, $\dot{\mathbf{q}}''$ is the heat-flux vector, and $\mathbf{H}$ is the vector of body forces. The specific total energy $E$ is obtained as

$$E = h + \frac{|\mathbf{v}|^2}{2} - \frac{p}{\rho} \tag{3}$$

Thermodynamic polynomials are used for calculating the specific heats of individual gas components [19]. The mixture specific heat is obtained by mass-fraction weighting of each species. The ideal-gas equation of state is employed for closing the preceding formulation. Radiation heat transfer is considered for both phases. For the continuous phase, to account for the radiation due to the participating media, the discrete ordinates method is employed. The radiation spectrum used is the gray thermal radiation for modeling diffuse, wavelength-independent radiation [7].

### B. Dispersed Phase

In the current Lagrangian multiphase model, particlelike elements known as parcels are followed through the continuum. The state of each parcel is updated according to a selected set of models [18]. The material particles are represented as either single-component (Al) or multicomponent ($Al/Al_2O_3$) particles with constant density. The particle motion is governed by the momentum and energy-conservation equations, which include drag and convective heat transfer, respectively. A mass-conservation equation is solved to account for the change of the Al droplet mass due to evaporation/combustion:

$$\frac{\mathrm{d}m_p}{\mathrm{d}t} = \dot{m}_p \tag{4}$$

where $m_p$ is the droplet mass. The rate of mass transfer $\dot{m}_p$ is accumulated over all the parcels, and applied in the continuous-phase continuity equation.

The equation of conservation of momentum for a material particle is

$$m_p \frac{\mathrm{d}\mathbf{v}_p}{\mathrm{d}t} = \mathbf{F}_s + \mathbf{F}_b \tag{5}$$

Here, $\mathbf{F}_s$ represents the forces acting on the droplet surface, and $\mathbf{F}_b$ represents the body forces. The former includes the effect of drag and pressure force, whereas the latter contains the effect of gravity. The momentum transfer to the particle from the continuous phase is simply $\mathbf{F}_s$. This is accumulated over all the parcels, and applied in the continuous-phase momentum equation. The drag force is given by

$$\mathbf{F}_d = \frac{1}{2} C_d \rho A_p |\mathbf{v}_s| \mathbf{v}_s \tag{6}$$

where $C_d$ is the drag coefficient of the particle, $\mathbf{v}_s$ is the particle slip velocity, and $A_p$ is the projected area of the particle. The pressure force is given by

$$\mathbf{F}_p = -V_p \nabla p_{\mathrm{static}} \tag{7}$$

where $V_p$ is the volume of the particle, and $\nabla p_{\mathrm{static}}$ is the gradient of the static pressure in the continuous phase.

The particles are assumed to be internally homogeneous, that is, the Biot number is less than ~0.1. The energy-conservation equation consistent with this assumption takes the following form:

$$m_p c_p \frac{\mathrm{d}T_p}{\mathrm{d}t} = Q_t + Q_{\mathrm{rad}} \tag{8}$$

Here, $Q_t$ represents the rate of convective heat transfer to the particle from the continuous phase, and $Q_{\mathrm{rad}}$ is the rate of radiative heat transfer. The Ranz–Marshall correlation [20] is used to determine the heat-transfer coefficient. Particle radiation and turbulent dispersion are considered for the dispersed-phase droplets. The average absorption and scattering efficiency for the droplets was assumed to be 0.7 and 0.1, respectively.

### C. Al Droplet Combustion and Gas-Phase Reactions

To simulate the oxidation of $Al_{(l)}$ to $Al_2O_{3(g)}$, it was assumed that $Al_{(l)}$ first evaporates and then oxidizes to $Al_2O_{3(g)}$. The unburnt $Al_{(l)}$ particles evaporate [$Al_{(l)} \rightarrow Al_{(g)}$] at a rate based on the Hermsen correlation mentioned by Sabnis [9], followed by the rapid gas-phase oxidation to form $Al_2O_{3(g)}$. The correlation is given by

$$\frac{\mathrm{d}(\dot{m}_{\mathrm{Al}})}{\mathrm{d}t} = -\frac{\pi}{2} \rho_{\mathrm{Al}} \frac{k}{n} D_p^{3-n} \tag{9}$$

where the exponent $n$ is 1.8, and the burning-rate constant $k$ is given by

$$k = 8.3314 \times 10^{-5} A_k^{0.9} p_c^{0.27} \frac{Sh}{2} \tag{10}$$

In the aforementioned expression, $p_c$ is the absolute chamber pressure (psi), $Sh$ is the Sherwood number, and $A_k$ is a measure of the availability of oxidizing species. $A_k$ is computed using

$$A_k = 100 \sum_i X_i \tag{11}$$

where the subscript $i$ represents the $i$th oxidizing species. In the gas phase, the following two reactions are used:

$$2Al_{(g)} + 3H_2O \rightarrow Al_2O_{3(g)} + 3H_2 \tag{R1}$$

$$2Al_{(g)} + 3CO_2 \rightarrow Al_2O_{3(g)} + 3CO \tag{R2}$$

A standard eddy breakup (EBU) [18] model is used for the preceding reactions with EBU constant $A_{\mathrm{mix}} = 100$, so that the overall rate of Al consumption is dictated by the evaporation of $Al_{(l)}$ to $Al_{(g)}$.

### D. Mechanical-Erosion Rate

Based on the flow distribution obtained from the Eulerian–Lagrangian analysis, the next step is to predict and quantify the level of mechanical erosion. The erosion rate is defined as the mass of wall material eroded per unit area per unit time ($\mathrm{kg/m^2/s}$). It is calculated for the nozzle wall by accumulating the damage caused by the impact of each $Al/Al_2O_3$ particulate on the nozzle surface, and is given by

$$E_f = \frac{1}{A_f} \sum_{\pi(f)} \dot{m}_\pi e_r \tag{12}$$

in which $A_f$ is the nozzle-surface area, $\dot{m}_\pi$ is the mass flow rate of particles in parcel $\pi$ impinging on the face, and $e_r$ is the erosion ratio. The summation is made over all parcels, which impact the face at a given time step. The mechanical-erosion rate is thus determined by the particle impact on the wall and the erosion ratio. Among the various correlations available for the mechanical-erosion ratio $e_r$, those established by Neilson and Gilchrist [21,22] and Oka et al. [23] were found most suitable for the present study.

Neilson and Gilchrist [22] conducted experiments on a test rig developed to produce an erosion damage similar to that found in a rocket nozzle. The degree and pattern of the damage for a given nozzle material were found to depend on particle velocity, flow structure, and size and type of particles. The angle of attack of the particle stream on the wall played an important role in determining mechanical erosion. For hard, brittle substances, severe damages occur with normal impact, whereas for ductile materials, the maximum erosion took place when the angle of attack is small. Neilson and Gilchrist [21] performed further studies in which streams of particles of various materials were used to erode different material specimens. Measurements of wear were made to quantify the unknown coefficients $\phi$, $\varepsilon$, $K$, and $\alpha_0$ in the following correlation for the erosion ratio:

$$\begin{aligned} e_r &= \frac{U^2 \cos^2\alpha \sin n\alpha}{2\phi} + \frac{(U \sin\alpha - K)^2}{2\varepsilon} \alpha < \alpha_0 \\ e_r &= \frac{U^2 \cos^2\alpha}{2\phi} + \frac{(U \sin\alpha - K)^2}{2\varepsilon} \alpha \geq \alpha_0 \end{aligned} \tag{13}$$

where $\alpha$ is the particle incidence angle at the impact, and $2n\alpha_0 = \pi$. In the *preceding* correlations, the first and second terms on the right-hand side represent the cutting and deformation wear, respectively. Thus, $\phi$ is the cutting-wear coefficient and $\varepsilon$ is the deformation-wear coefficient. Neilson and Gilchrist [21] outlined a procedure for fitting this correlation to their experimental data. From the different combinations of the particle and target materials studied, of particular interest here are their data for graphite plates eroded by solid 297 $\mu$m alumina particles at $U_p = 110.6$ m/s. The empirical coefficients in Eq. (13), provided by Neilson and Gilchrist [21], have been calibrated and are summarized in Table 1. One limitation of the Neilson and Gilchrist correlation is that the set of coefficients is valid only for the range of the operating conditions considered in the measurements. No sufficient data were provided to indicate the sensitivity of these coefficients to particle velocity or size for $Al_2O_3$ on the graphite samples.

The erosion correlation of Oka et al. [23] and Oka and Yoshida [24] incorporates particle size and velocity variations more systematically, and is given by

**Table 1 Calibrated parameters for the Neilson and Gilchrist correlation [21]**

| Parameter | Value |
|---|---|
| $\phi$ | 215.7 kJ/kg |
| $\varepsilon$ | 95 kJ/kg |
| $K$ | 0 m/s |
| $n$ | 4.3 |

**Table 2 Calibrated parameters for the Oka correlation [23,24]**

| Parameter | Value |
|---|---|
| $U_{\mathrm{ref}}$ | 110.6 m/s |
| $D_{\mathrm{ref}}$ | 297 $\mu$m |
| $e_{\mathrm{ref}}$ | 0.065 |
| $H_v$ | 0.228 GPa |
| $n_1$ | 0.793 |
| $n_2$ | 0.762 |
| $k_2$ | 2.0 |
| $k_3$ | 0.0 |

$$e_r = g(\alpha)e_{\mathrm{ref}}\left(\frac{U}{U_{\mathrm{ref}}}\right)^{k_2}\left(\frac{D}{D_{\mathrm{ref}}}\right)^{k_3} \tag{14}$$

in which $U_{\mathrm{ref}}$ and $D_{\mathrm{ref}}$ are the particle velocity and diameter at reference conditions, respectively, and $e_{\mathrm{ref}}$ is the erosion ratio at normal incidence at reference conditions. The function $g(\alpha)$ describes the variation of erosion with the impact angle as

$$g(\alpha) = (\sin\alpha)^{n_1}[1 + H_v(1 - \sin\alpha)]^{n_2} \tag{15}$$

in which $H_v$ is the Vickers hardness in GPa. The unknowns in the preceding equations are the four coefficients $k_2$, $k_3$, $n_1$, and $n_2$. The purported advantage of the Oka correlation lies in the fact that neither $n_1$ nor $n_2$ is a function of particle velocity or size. Instead, they depend on material properties and particle shape. The Oka correlation can thus be used with more confidence at conditions other than the reference conditions. The challenge with the Oka correlation, however, is the acquisition of enough data to determine the four coefficients. From the Neilson and Gilchrist data [21], we choose $U_{\mathrm{ref}} = 110.6$ m/s, $D_{\mathrm{ref}} = 297$ $\mu$m, and $e_{\mathrm{ref}} = 0.065$. The angle function $g(\alpha)$ is fitted to the Neilson and Gilchrist data with an assumed hardness for graphite as $H_v = 0.228$ GPa, yielding the parameters summarized in Table 2. This appears to be as much as can be extracted from the available data, and the values of $k_2$ and $k_3$ cannot be determined. Ideally, measurements of the normal erosion ratio should be made for an extensive range of particle sizes and velocities. In the absence of such data, $k_2$ and $k_3$ are assumed to take their theoretical values [23], namely, 2.0 and 0.0, respectively. Because this removes the particle-size effect, the resulting correlation involves uncertainties in this regard. Figure 1 shows a comparison of the correlations with the reference experimental data used to obtain them.

As with any empirical correlation, caution must be exercised when employing Eqs. (13) and (14) beyond their range of validity. In the present work, such a range is limited to conditions close to the particle sizes (50–300 $\mu$m) and impact velocities on the nozzle surface (in the order of ~100 m/s) for which the coefficients are obtained. Oka et al. [23] and Oka and Yoshida [24] studied the impact of solid particles as well as liquid droplets [25]. A velocity exponent of 2.0 was obtained for droplet velocities of more than 100 m/s, which supports the use of $k_2 = 2.0$ in the present analysis. They further indicated that, similar to the situation with solid particles, the erosion damage by liquid droplets is related to the energy of impinging droplets in the high-velocity region. It should be noted that, in the case of solid rocket motors, the $Al_2O_3$ particles are mostly present in the liquid phase with an oxide shell. The use of solid $Al_2O_3$ data for liquid particulates is one of the restrictive assumptions of the current study. The predictions so obtained will represent an upper limit, or the worst-case scenario, for mechanical-erosion rates.

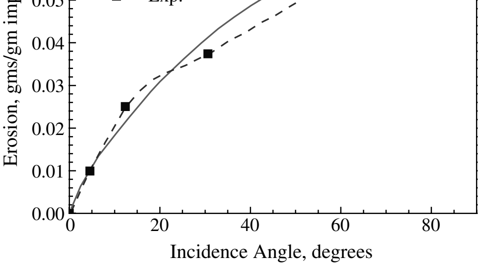

**Fig. 1 Comparison of derived correlations and experimental data (297 $\mu$m solid $Al_2O_3$ particles on graphite plate); Exp. denotes experiment.**

## III. Numerical Methods

The continuous-phase conservation equations are solved using the coupled solver [18]. The algorithm yields robust and accurate solutions for compressible flows. The flowfield inside a rocket motor spans a broad range of Mach numbers (0.0–3.0). To deal with such a flow, a preconditioning scheme is necessary for maintaining numerical accuracy and efficiency. To provide an efficient solution of the flowfield at all speeds, a preconditioning matrix is incorporated into Eq. (1) as follows [26,27]:

$$\Gamma\frac{\partial}{\partial t}\left[\int_V \mathbf{Q}\,\mathrm{d}V + \oint(\mathbf{F} - \mathbf{G})\cdot \mathrm{d}\mathbf{a}\right] = \int_V \mathbf{H}\,\mathrm{d}V \tag{16}$$

where $\Gamma$ is the appropriate preconditioning matrix, and $\mathbf{Q}$ is the dependent vector of primary variables represented by

$$\mathbf{Q} = [\,p \quad \mathbf{v} \quad T\,]^T \tag{17}$$

The convective fluxes in Eq. (16) are evaluated by a second-order upwind, flux-difference splitting scheme [26,28]. With a matrix dissipation term added to the fluxes, the numerical scheme not only performs well at higher speeds, but also provides the pressure–velocity coupling required for numerical stability and efficient convergence at low speeds. Time integration is performed using implicit discretization of the governing equations, combined with a Newton-type linearization of all fluxes. Turbulence closure is achieved using the standard $k$-$\varepsilon$ two-equation model that involves transport equations for the turbulent kinetic energy and its dissipation rate. The transport equations are of the form suggested by Jones and Lander [29]. For boundary-layer flows with surface transpiration, as encountered in the present study, the two-equation model leads to solutions that show reasonable agreement with those obtained from more comprehensive models, such as large-eddy simulations [30–34].

## IV. Model Assumptions and Input Conditions

For the aluminized AP/HTPB propellant, the multicomponent gas-phase flow inside the motor is composed mainly of $H_2O$, $Al_2O_3$, Al, $CO_2$, HCL, CO, $N_2$, and $H_2$ [17]. Only a sector of the motor in the azimuthal direction is simulated using periodic boundary conditions, due to the rotational symmetry. The combustion-chamber pressure and temperature are used as the inlet stagnation conditions for the nozzle flow. In the current study, the geometry employed is similar to the ballistic test and evaluation system (BATES) motor at the initial grain configuration, adopted from Sabnis [9]. The overall length of the motor is about 2 m, with the nozzle section starting at 1.52 m. The axisymmetric computational grid is composed of $140 \times 60$ cells in the axial and radial directions, respectively. The grid points were clustered appropriately at the wall and in the nozzle section. The final mesh, which is similar to the one employed by Sabnis [9], was reached after conducting grid-independence studies. The propellant is composed of AP/HTPB/Al with a mass ratio of 71/14/15. Considering the propellant burning rate of 9.0678 mm/s and propellant density of 1.794 g/cm$^3$ [9], the total burning mass flux is 16.273 kg/m$^2$/s. The chamber pressure is 6.8 MPa and the chamber temperature is 3327 K. The motor head end is treated as adiabatic while the nozzle-surface temperature is fixed at 2500 K. In reality, the nozzle inner-surface temperature may vary axially in the

**Table 3 Gas-phase[a] (Eulerian) inlet conditions**

| Species | Mass fraction |
|---|---|
| $H_2O_{(g)}$ | 0.114 |
| $CO_{(g)}$ | 0.281 |
| $CO_{2(g)}$ | 0.032 |
| $H_{2(g)}$ | 0.022 |
| $Al_{(g)}$ | 0.000 |
| $Al_2O_{3(g)}$ | 0.219 |
| $HCl_{(g)}$ | 0.232 |
| $N_{2(g)}$ | 0.100 |
| Inlet flow conditions | |
| $p_0$ | 68 MPa |
| $T_0$ | 3327 K |

[a] Gas-phase inlet mass flux is 15.199 $kg/m^2/s$, which excludes 10% (0.244 $kg/m^2/s$) unburnt Al and 20% (0.830 $kg/m^2/s$) $Al_2O_3$ droplets.

**Table 4 Dispersed-phase (Lagrangian) inlet conditions**

| Species | Mass flux, $kg/m^2/s$ | Injection temperature, K | Droplet diameter, $\mu$m | Injection velocity, m/s |
|---|---|---|---|---|
| Single-component $Al_{(l)}$ | 0.122 | 950 | 50 | 0.1 (Vertically downward) |
| Multicomponent $Al_{(l)}/Al_2O_{3(l)}$ | 0.122/ 0.830 | 2350 | Log-normal distribution mean: 100; $\log_{10}$ standard deviation: 0.2 | 0.1 (Vertically downward) |

range of ~2200–2800 K, depending on the propellant and nozzle configuration employed [5]. An average value of 2500 K is a reasonable approximation for the current scenario.

It is assumed that 10% (0.244 $kg/m^2/s$) of Al remains unburnt at the propellant surface. The remaining Al burns completely to form $Al_2O_3$. To get the initial mass fractions of species at the burning surface, an equilibrium concentration was determined for the AP/HTPB/Al (71/14/13.5 by mass) propellant composition (assuming 10% Al remains unburnt) from the chemical-equilibrium analysis [35]. The $Al_2O_3$ particles consist of approximately 80% by mass of submicron $Al_2O_3$ mist, which is modeled as part of the continuous phase. The remaining 20% $Al_2O_3$ particles are present as an oxide cap on Al droplets (i.e., as multicomponent $Al/Al_2O_3$ droplets), and are treated using the Lagrangian formulation [9,10]. The size distribution of $Al/Al_2O_3$ droplets was taken as log normal, with a mean of 100 $\mu$m and a $\log_{10}$ standard deviation of 0.2 [9]. Out of the 10% unburnt Al, it is assumed that 50% (0.122 $kg/m^2/s$) is present as pure Al droplets, which burn to form an alumina mist as they travel through the chamber, whereas the remaining 50% has an oxide-shell cap of $Al_2O_3$. Based on the assumptions, the multicomponent $Al/Al_2O_3$ droplet is composed of 13% Al and 87% $Al_2O_3$ by mass. The presence of $Al_2O_3$ oxide-shell cap hinders the further oxidation of Al, resulting in a very low or negligible oxidation rate of the Al core. Based on the preceding calculations, Tables 3 and 4 summarize the input conditions for the Eulerian and Lagrangian phases.

The gas-phase combusting species (Table 3), and the dispersed-phase $Al_{(l)}/Al_2O_{3(l)}$ and $Al_{(l)}$ droplets (Table 4) are injected along the side wall of the rocket-motor chamber to simulate the propellant burning behavior. The inward injection velocity of the droplets is 0.1 m/s, which is about 3% of the gas velocity at the propellant surface. Madabhushi et al. [36] indicated that the particle dynamics are insensitive to the droplet injection velocity in the range of 1–25% of the gas velocity. In the present work, particles are assumed to collide with the nozzle surface, and bounce off with normal and tangential restitution coefficients of unity.

## V. Results and Discussion

The combined Eulerian–Lagrangian approach outlined in the previous sections was applied to simulate the steady-state two-phase flowfield inside the BATES rocket motor. The governing equations were solved by employing the commercially available CFD code STAR-CCM+ [18]. The Lagrangian treatment includes turbulent dispersion, droplet evaporation, drag forces, and two-way coupling of mass and energy transfer between droplets and the continuous phase. The calculations were initiated by specifying the mass flux at the propellant surface. Figure 2 shows the distributions of Mach number, temperature, pressure, and velocity magnitude within the rocket motor. The flow is supersonic at the nozzle exit, with a Mach number reaching 2.65. The area-averaged temperature and pressure on the transverse plane at the nozzle exit are 1833 K and 1.89 bar, respectively.

Figure 3 shows the single-component $Al_{(l)}$ droplet trajectories displaying the particle mass and temperature. A total of 700 $Al_{(l)}$ parcels were injected along the propellant surface. The $Al_{(l)}$ droplets burn at a rate given by Eq. (9) as they traverse the chamber. The temperature of $Al_{(l)}$ droplets continues to rise above their injection

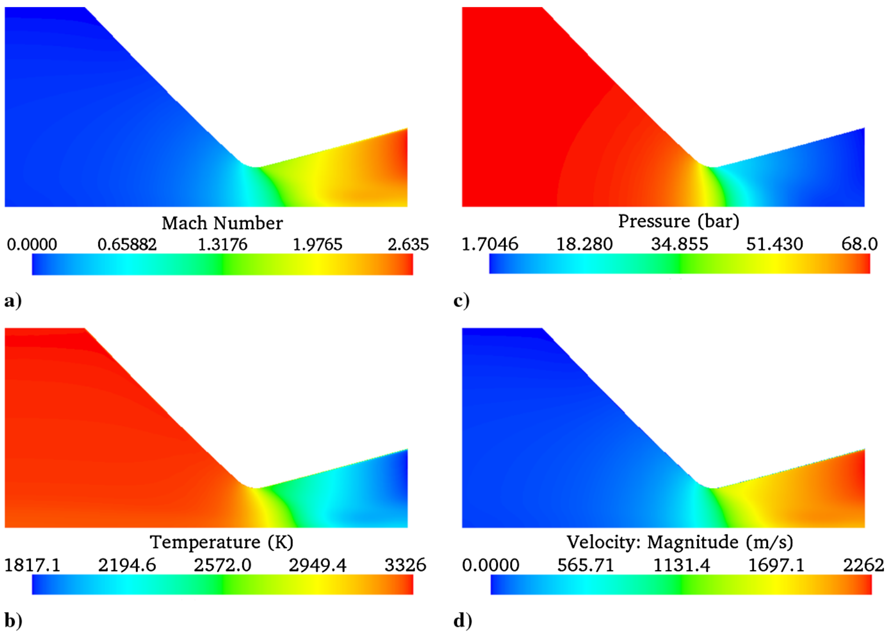

**Fig. 2 Distributions of a) Mach number, b) temperature, c) pressure, and d) velocity magnitude in a rocket motor.**

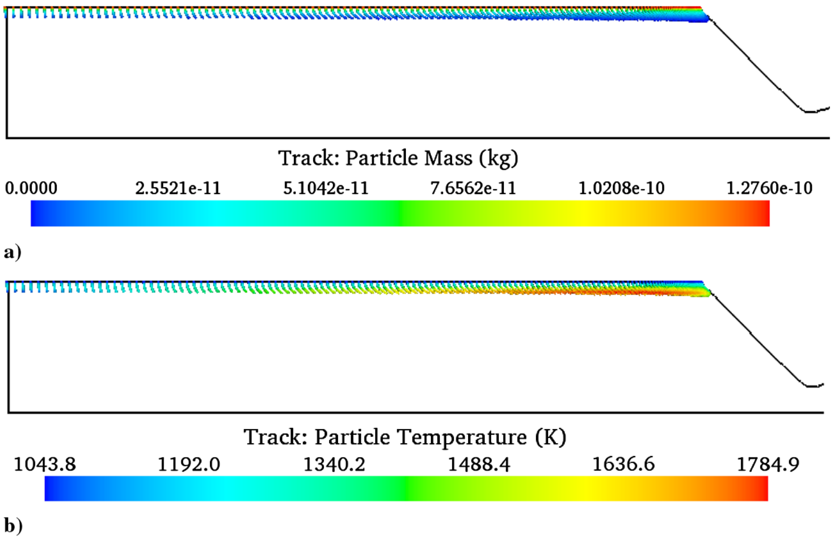

**Fig. 3** **Trajectories of burning $Al_{(l)}$ droplets showing a) particle mass and b) particle temperature.**

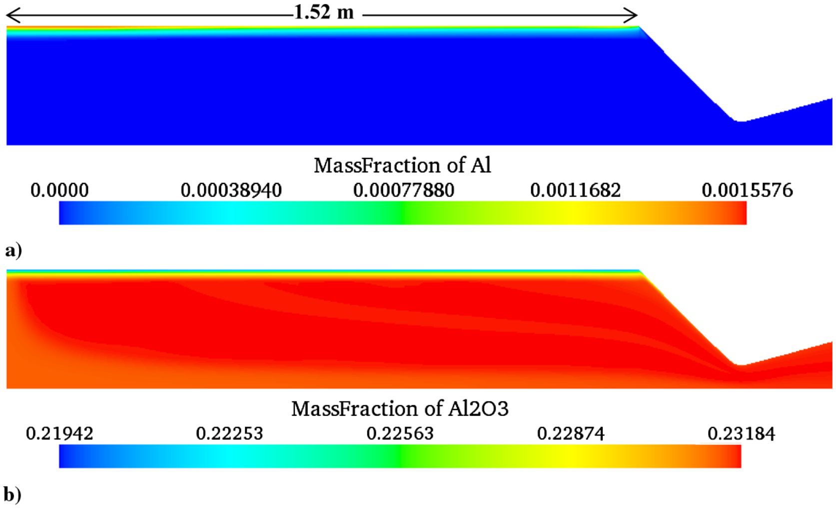

**Fig. 4** **Distributions of mass fractions of a) $Al_{(g)}$ and b) $Al_2O_{3(g)}$ in the gas phase.**

temperature of 950 K, and they are consumed within a short distance from the propellant surface. None of them lasts enough to impinge on the nozzle surface. Thus, no mechanical erosion is caused by the single-component $Al_{(l)}$ droplets. The evaporated Al reacts with the $H_2O$ and $CO_2$ species to form the gaseous $Al_2O_3$ mist and other products according to reactions (R1) and (R2). Figure 4 shows the distributions of the mass fractions of $Al_{(g)}$ and $Al_2O_{3(g)}$. The presence of $Al_{(g)}$ in the gas phase results from the evaporation close to the propellant surface. The mass fraction of $Al_2O_{3(g)}$ increases due to its formation through reactions (R1) and (R2). Because the Al droplet consumption occurs closer to the propellant surface, the mass fractions of combustion species in the core region remain relatively unaffected.

Figure 5 shows the multicomponent $Al_{(l)}/Al_2O_{3(l)}$ droplet trajectories, displaying the particle diameter and velocity magnitude. A sufficiently large number of $Al/Al_2O_3$ Lagrangian parcels were chosen to ensure that erosion results were independent of the number of parcels injected. In conducting the analyses, the number of parcels was progressively increased to 3500. Above 3500 parcels, the difference in the computed mechanical-erosion rates was insignificant. The injected particle-diameter distribution is log normal, as summarized in Table 4. Figure 5a indicates the droplet diameters in the range of 50–180 $\mu$m. Because the Al in the multicomponent droplets is assumed to be covered by an $Al_2O_3$ oxide-shell cap, the droplets do not burn and their mass remains constant. Figure 5b shows that the particle velocities increase rapidly as they progress through the rocket nozzle. The droplets rebounding from the axis of symmetry of the motor are effectively in perfect collision with identical droplets originating from the opposite side of the rocket motor.

Figure 6 shows the dispersed-phase $Al_{(l)}/Al_2O_{3(l)}$ droplets displaying particle temperatures and residence times. The droplet temperature increases from the injection temperature of 2350 K to about 3277 K in the chamber. Individual particles heat up to different temperatures, depending on the trajectories they follow and the corresponding residence times inside the motor. Particles with longer residence times achieve relatively higher temperatures. Figure 7 shows a close-up view of the $Al_{(l)}/Al_2O_{3(l)}$ particle trajectories and their velocity magnitudes. The particles appear to impinge only on the convergent section of the nozzle surface. No mechanical erosion is thus anticipated at the nozzle throat and its downstream region. The impinging velocity is about $\sim$100 m/s, close to the value used by Neilson and Gilchrist in their experiments [21,22]. These trajectories, however, depend on the particle mass. Lighter particles follow the gas-phase flow more closely than the heavier ones, as evident in Fig. 5a.

Figure 8 shows the incident mass flux of $Al_{(l)}/Al_2O_{3(l)}$ particles on the nozzle surface, represented by the term $\dot{m}_\pi$ in Eq. (12). The net

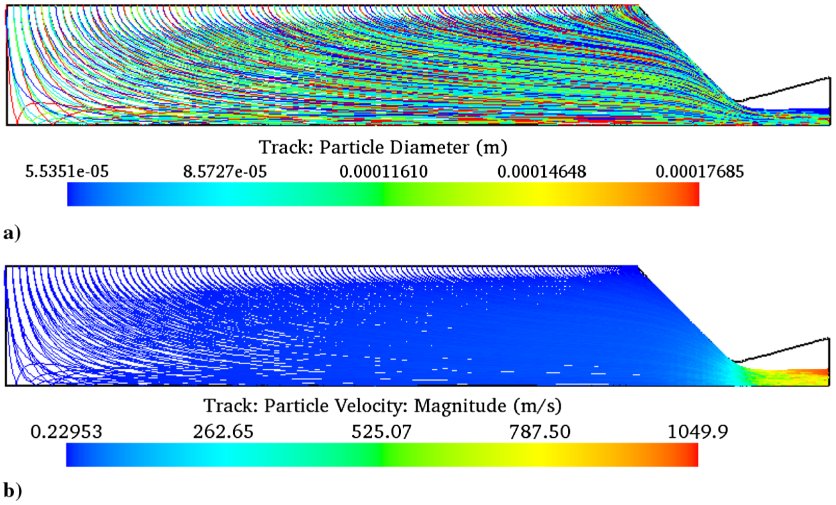

**Fig. 5** **Multicomponent $Al_{(l)}/Al_2O_{3(l)}$ droplet trajectories showing a) particle diameter and b) particle velocity magnitude.**

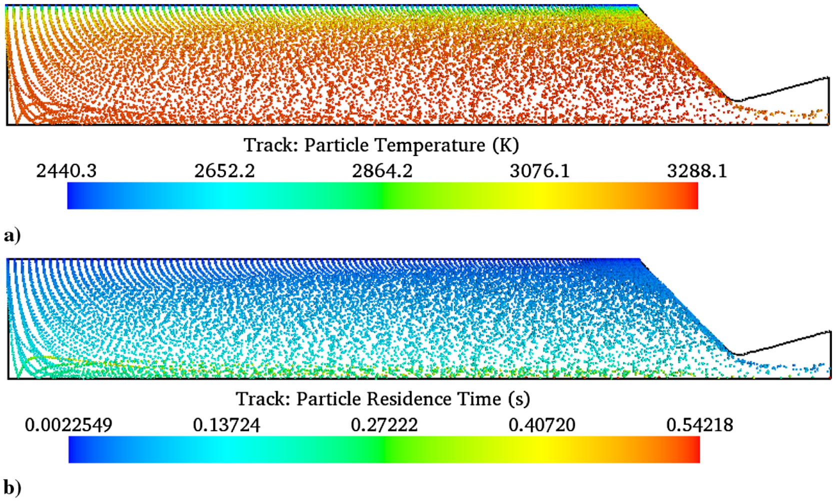

**Fig. 6** **Dispersed multicomponent $Al_{(l)}/Al_2O_{3(l)}$ droplets showing a) particle temperature and b) particle residence time.**

mechanical-erosion rate, however, is determined by not only the incident mass flux of particles, but also their size, velocity, and impact angle. Figure 9 shows the distribution of the mechanical-erosion rate of the nozzle surface due to particle impingement, based on the Neilson and Gilchrist correlation [21]. Figure 10 shows the predicted mechanical-erosion rate in accordance with the Oka correlation [23,24]. The erosion reaches its maximum in the convergent section of the nozzle in both cases. Figure 11 shows the corresponding variations of the erosion rate along the nozzle surface for the two correlations. For the Neilson and Gilchrist correlation, a peak erosion-rate value of 0.0586 $kg/m^2/s$ occurs around 1.736 m along the motor axis from the head end. Assuming a graphite-nozzle-material density of 1.8 $g/cm^3$, the erosion rate is around 1.281 mil/s. For the Oka correlations, a peak value of 0.0619 $kg/m^2/s$ (1.354 mil/s) is also observed around 1.736 m along the motor axis. No mechanical erosion is observed at the nozzle throat

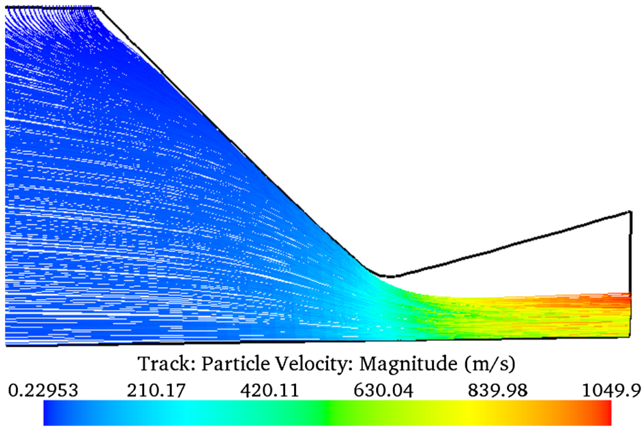

**Fig. 7** **Multicomponent $Al_{(l)}/Al_2O_{3(l)}$ trajectories in a rocket nozzle.**

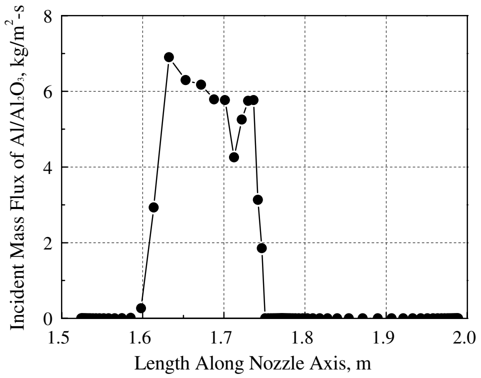

**Fig. 8** **Incident mass flux due to $Al_{(l)}/Al_2O_{3(l)}$ particle impingement on the nozzle surface.**

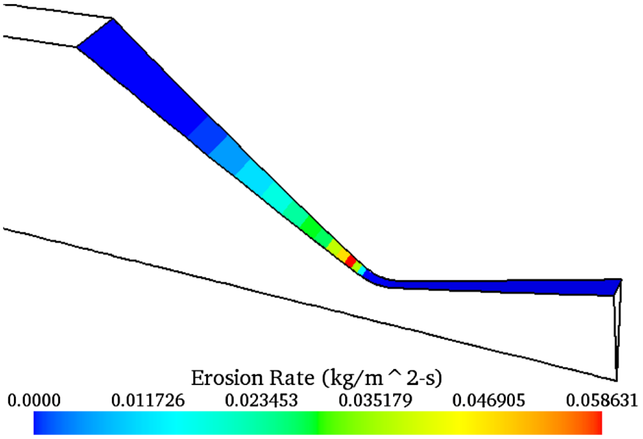

**Fig. 9 Distribution of the mechanical-erosion rate of the nozzle due to $Al_{(l)}/Al_2O_{3(l)}$ particle impingement; based on the Neilson and Gilchrist correlation [21].**

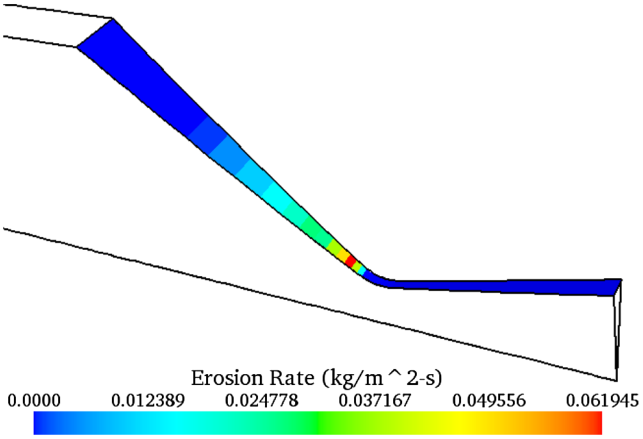

**Fig. 10 Distribution of the mechanical-erosion rate of the nozzle due to $Al_{(l)}/Al_2O_{3(l)}$ particle impingement; based on the Oka correlation [23,24].**

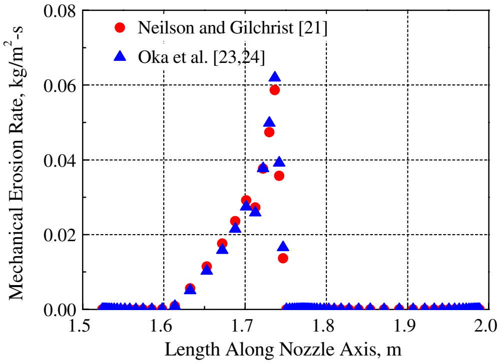

**Fig. 11 Mechanical-erosion rate of the nozzle surface; based on the Neilson and Gilchrist [21] and Oka et al. [23,24] correlations.**

(~1.77 m) or downstream, because the particle trajectories move away from the surface in those regions. Thus, any erosion occurring at the nozzle throat and its downstream region is practically caused by chemical means.

**Table 5 Maximum mechanical-erosion rates**

| Correlation | Erosion rate, $kg/m^2/s$ | Erosion rate,[a] mil/s |
|---|---|---|
| Neilson and Gilchrist [21] | 0.0586 | 1.281 |
| Oka et al. [23,24] | 0.0619 | 1.354 |

[a] Assuming graphite-nozzle-material density of 1.8 $g/cm^3$.

Both the Neilson and Gilchrist [21] and Oka correlations [23,24] lead to similar distributions of the mechanical-erosion rate, and their maximum values are close to each other. Such results are expected, given that both correlations were calibrated using the same experimental data. Table 5 summarizes the overall results. Experimental data on mechanical-erosion rates obtained for different rocket motors with carbon-based nozzles vary from 0.0 to 3.5 mil/s [37]. The calculated mechanical-erosion rates in the present study fall within this range. It is worth noting that the predicted erosion rates are valid only for the flow conditions for which the employed correlations are established. With suitable and reliable data and correlations, the current framework and methodology can be applied to accurately predict the mechanical-erosion rate for any rocket-motor configuration.

## VI. Conclusions

A theoretical/numerical analysis has been established to predict the mechanical erosion of graphite-nozzle materials in solid rocket motors. The propellant considered is ammonium perchlorate/aluminum (Al)/hydroxyl-terminated polybutadiene (71/15/14 by mass) composite propellant. The multicomponent gas-phase dynamics is modeled using the Eulerian conservation equations of mass, momentum, and energy. The dispersed phase, consisting of single-component Al and multicomponent Al/aluminum oxide ($Al_2O_3$) droplets, is treated using the Lagrangian framework. An aluminum-droplet combustion is considered, with $Al_{(l)}$ oxidizing to $Al_2O_{3(g)}$. The interactions between the gas and particle phases are modeled by considering the effects of interphase mass, momentum, and energy transfer. In addition, particle radiation and turbulent dispersion are taken into account for the multicomponent $Al/Al_2O_3$ droplets.

Based on the experimental data of the $Al_2O_3$ particle impact on graphite plates, a methodology was developed to quantitatively predict the mechanical-erosion rate. Two different correlations were calibrated and employed to determine the mechanical-erosion rate for a rocket nozzle. Results fall in the range of available experimental data. Mechanical erosion is prevalent only in the convergent section of the rocket nozzle because the particle trajectories move away from the surface at the nozzle throat and its downstream region. Although the flowfield inside the rocket motor is treated in a comprehensive manner, the calculated erosion rates are valid only for the flow conditions for which the material-erosion correlations are established.

## Acknowledgments

The authors thank CD-adapco, Ltd. for allowing the use of the computational fluid dynamics software STAR-CCM+. This work was partly supported by the William R. T. Oakes Endowment at the Georgia Institute of Technology, and partly by the Office of Naval Research as a part of a Multidisciplinary University Research Initiative project funded under contract N00014-04-1-0683.

## References

[1] Swope, L. W., and Berard, M. F., "Effects of Solid-Rocket Propellant Formulations and Exhaust-Gas Chemistries on the Erosion of Graphite Nozzles," *AIAA Solid Propellant Rocket Conference*, Palo Alto, CA, Jan. 1964.

[2] Geisler, R. L., "The Relationship Between Solid Propellant Formulation Variables and Nozzle Recession Rates," *JANNAF Rocket Nozzle Technology Subcommittee Workshop*, Lancaster, CA, 1978.

[3] Sutton, G. P., and Biblarz, O., *Rocket Propulsion Elements*, 7th ed., Wiley InterScience, New York, 2001, pp. 552–562.

[4] Geisler, R. L., "A Global View of the Use of Aluminum Fuel in Solid Rocket Motors," AIAA Paper 2002-3748, July 2002.

[5] Thakre, P., and Yang, V., "Chemical Erosion of Carbon–Carbon/Graphite Nozzles in Solid-Propellant Rocket Motors," *Journal of Propulsion and Power*, Vol. 24, No. 4, 2008, pp. 822–833. doi:10.2514/1.34946

[6] Thakre, P., and Yang, V., "Chemical Erosion of Refractory Metal Nozzle Inserts in Solid-Propellant Rocket Motors," *Journal of Propulsion and*

*Power*, Vol. 25, No. 1, 2009, pp. 40–50. doi:10.2514/1.37922

[7] Thakre, P., and Yang, V., "Effect of Surface Roughness and Radiation on Graphite Nozzle Erosion in Solid Rocket Motors," *Journal of Propulsion and Power*, Vol. 28, No. 2, 2012, pp. 448–451. doi:10.2514/1.57841

[8] Thakre, P., and Yang, V., "Mitigation of Graphite Nozzle Erosion by Boundary Layer Control in Solid Propellant Rocket Motors," *Journal of Propulsion and Power*, Vol. 25, No. 5, 2009, pp. 1079–1085. doi:10.2514/1.41293

[9] Sabnis, J., "Numerical Simulation of Distributed Combustion in Solid-Rocket Motor with Metallized Propellant," *Journal of Propulsion and Power*, Vol. 19, No. 1, 2003, pp. 48–55. doi:10.2514/2.6101

[10] Dupays, J., "Two-Phase Unsteady Flow in Solid Rocket Motors," *Aerospace Science and Technology*, Vol. 6, No. 6, 2002, pp. 413–422. doi:10.1016/S1270-9638(02)01182-3

[11] Kato, K., Ueno, K., and Sawada, K., "Estimation of Mechanical Erosion at Nozzle Inlet by Multiphase Flow Simulation in Solid Rocket Motor Considering Aluminum Droplets and Alumina Mist," AIAA Paper 2007-341, Jan. 2007.

[12] Shimada, T., Daimon, Y., and Sekino, N., "Numerical Simulation of Flow Inside a Solid Rocket Motor by Eulerian-Hybrid Approach with Relation to Nozzle Inlet Ablation," *Proceedings of the 8th International Symposium on Experimental and Computational Aerothermodynamics of Internal Flows*, Lyon, July 2007.

[13] Culick, F. E. C., and Yang, V., "Prediction of the Stability of Unsteady Motions in Solid Propellant Rocket Motors," *Nonsteady Burning and Combustion Stability of Solid Propellants*, edited by DeLuca, L., and Summerfield, M., Vol. 143, Progress in Astronautics and Aeronautics, AIAA, Washington, DC, 1992, pp. 719–779, Chap. 18.

[14] Cai, W. D., Ma, F. H., and Yang, V., "Two-Phase Flow Interactions in Solid-Propellant Rocket Motors with Acoustic Oscillations," *Journal of Propulsion and Power*, Vol. 19, No. 3, 2003, pp. 385–396. doi:10.2514/2.6142

[15] Yang, V., Brill, T., and Ren, W. Z. (eds.), "Combustion Dynamics of Homogeneous Solid Propellant in Rocket Motor with Acoustic Excitations," *Solid-Propellant Chemistry, Combustion, and Motor Interior Ballistics*, Vol. 185, Progress in Astronautics and Aeronautics, AIAA, Reston, VA, 2000, pp. 885–905.

[16] Beckstead, M. W., Puduppakkam, K., Thakre, P., and Yang, V., "Modeling of Combustion and Ignition of Solid-Propellant Ingredients," *Progress in Energy and Combustion Science*, Vol. 33, No. 6, 2007, pp. 497–551. doi:10.1016/j.pecs.2007.02.003

[17] Cai, W. D., Thakre, P., and Yang, V., "A Model of AP/HTPB Composite Propellant Combustion in Rocket Motor Environments," *Combustion Science and Technology*, Vol. 180, No. 12, 2008, pp. 2143–2169. doi:10.1080/00102200802414915

[18] STAR-CCM+, Ver. 6.06, CD-adapco Ltd., Melville, NY, Oct. 2011, http://www.cd-adapco.com.

[19] Roh, T. S., Tseng, I. S., and Yang, V., "Effects of Acoustic Oscillations on Flame Dynamics of Homogeneous Propellants in Rocket Motors," *Journal of Propulsion and Power*, Vol. 11, No. 4, 1995, pp. 640–650. doi:10.2514/3.23889

[20] Ranz, W. E., and Marshall, W. R., "Evaporation from Drops: Parts I and II," *Chemical Engineering Progress*, Vol. 48, No. 3, 1952, pp. 141–146.

[21] Neilson, J. H., and Gilchrist, A., "Erosion by a Stream of Solid Particles," *Wear*, Vol. 11, No. 2, 1968, pp. 111–122.

[22] Neilson, J. H., and Gilchrist, A., "An Experimental Investigation into Aspects of Erosion in Rocket Motor Nozzles," *Wear*, Vol. 11, No. 2, 1968, pp. 123–143.

[23] Oka, Y. I., Okamura, K., and Yoshida, T., "Practical Estimation of Erosion Damage Caused by Solid Particle Impact. Part 1: Effects of Impact Parameters on a Predictive Equation," *Wear*, Vol. 259, Nos. 1–6, 2005, pp. 95–101. doi:10.1016/j.wear.2005.01.039

[24] Oka, Y. I., and Yoshida, T., "Practical Estimation of Erosion Damage Caused by Solid Particle Impact. Part 2: Mechanical Properties of Materials Directly Associated with Erosion Damage," *Wear*, Vol. 259, Nos. 1–6, 2005, pp. 102–109. doi:10.1016/j.wear.2005.01.040

[25] Oka, Y. I., Mihara, S., and Miyata, H., "Effective Parameters for Erosion Caused by Water Droplet Impingement and Applications to Surface Treatment Technology," *Wear*, Vol. 263, Nos. 1–6, 2007, pp. 368–394. doi:10.1016/j.wear.2006.11.022

[26] Weiss, J. M., and Smith, W. A., "Preconditioning Applied to Variable and Constant Density Flows," *AIAA Journal*, Vol. 33, No. 11, 1995, pp. 2050–2057. doi:10.2514/3.12946

[27] Hsieh, S. Y., and Yang, V., "A Preconditioned Flux-Differencing Scheme for Chemically Reacting Flows at All Mach Numbers," *International Journal of Computational Fluid Dynamics*, Vol. 8, No. 1, 1997, pp. 31–49. doi:10.1080/10618569708940794

[28] Weiss, J. M., Maruszewski, J. P., and Smith, W. A., "Implicit Solution of Preconditioned Navier–Stokes Equations Using Algebraic Multigrid," *AIAA Journal*, Vol. 37, No. 1, 1999, pp. 29–36. doi:10.2514/2.689

[29] Jones, W. P., and Lander, B. E., "The Prediction of Laminarization with a Two-Equation Model of Turbulence," *International Journal of Heat and Mass Transfer*, Vol. 15, No. 2, 1972, pp. 301–314. doi:10.1016/0017-9310(72)90076-2

[30] Tseng, I. S., and Yang, V., "Combustion of a Double-Base Homogeneous Propellant in a Rocket Motor," *Combustion and Flame*, Vol. 96, No. 4, 1994, pp. 325–342. doi:10.1016/0010-2180(94)90102-3

[31] Apte, S., and Yang, V., "Turbulent Flame Dynamics of Homogeneous Solid Propellant in a Rocket Motor," *Proceedings of the Combustion Institute*, Vol. 28, No. 1, 2000, pp. 903–910. doi:10.1016/S0082-0784(00)80296-9

[32] Apte, S., and Yang, V., "Unsteady Flow Evolution in a Porous Chamber with Surface Mass Injection, I: Free Oscillation," *AIAA Journal*, Vol. 39, No. 8, 2001, pp. 1577–1586. doi:10.2514/2.1483

[33] Apte, S., and Yang, V., "Unsteady Flow Evolution in a Porous Chamber with Surface Mass Injection, II: Acoustic Excitation," *AIAA Journal*, Vol. 40, No. 2, 2002, pp. 244–253. doi:10.2514/2.1666

[34] Apte, S., and Yang, V., "A Large-Eddy Simulation Study of Transition and Flow Instability in a Porous-Walled Chamber with Mass Injection," *Journal of Fluid Mechanics*, Vol. 477, 2003, pp. 215–225. doi:10.1017/S0022112002002987

[35] Gordon, S., and McBride, B. J., "Computer Program for Calculation of Complex Chemical Equilibrium Compositions and Applications: I. Analysis," NASA, Rept. 1311, 1994.

[36] Madabhushi, R. K., Sabnis, J. S., de Jong, F. J., and Gibeling, H. J., "Calculation of Two-Phase Aft-Dome Flowfield in Solid Rocket Motors," *Journal of Propulsion and Power*, Vol. 7, No. 2, 1991, pp. 178–184. doi:10.2514/3.23310

[37] Ketner, D. M., and Hess, K. S., "Particle Impingement Erosion," AIAA Paper 1979-1250, June 1979.

K. Frendi
*Associate Editor*